nature SUPPLEMENTARY INFORMATION
https://doi.org/10.1038/s41586-018-0691-0

Efficient and stable emission of warm-white light from lead-free halide double perovskites

Jiajun Luo[1,11], Xiaoming Wang[2,11], Shunran Li[1,11], Jing Liu[1,11], Yueming Guo[3], Guangda Niu[1], Li Yao[1], Yuhao Fu[4], Liang Gao[1,5], Qingshun Dong[6], Chunyi Zhao[7], Meiying Leng[1], Fusheng Ma[6], Wenxi Liang[1], Liduo Wang[6], Shengye Jin[7], Junbo Han[8], Lijun Zhang[4], Joanne Etheridge[3,9], Jianbo Wang[10], Yanfa Yan[2]*, Edward H. Sargent[5] & Jiang Tang[1]*

---

[1]Sargent Joint Research Center, Wuhan National Laboratory for Optoelectronics (WNLO) and School of Optical and Electronic Information, Huazhong University of Science and Technology (HUST), Wuhan, China. [2]Department of Physics and Astronomy and Wright Center for Photovoltaics Innovation and Commercialization, The University of Toledo, Toledo, OH, USA. [3]Department of Materials Science and Engineering, Monash University, Clayton, Victoria, Australia. [4]State Key Laboratory of Superhard Materials, Key Laboratory of Automobile Materials of MOE, and School of Materials Science and Engineering, Jilin University, Changchun, China. [5]Department of Electrical and Computer Engineering, University of Toronto, Toronto, Ontario, Canada. [6]Key Laboratory of Organic Optoelectronics and Molecular Engineering of Ministry of Education, Department of Chemistry, Tsinghua University, Beijing, China. [7]State Key Laboratory of Molecular Reaction Dynamics and Collaborative Innovation Center of Chemistry for Energy Materials (iChEM), Dalian Institute of Chemical Physics, Chinese Academy of Sciences, Dalian, China. [8]Wuhan National High Magnetic Field Center, Huazhong University of Science and Technology (HUST), Wuhan, China. [9]Monash Centre for Electron Microscopy, Monash University, Clayton, Victoria, Australia. [10]School of Physics and Technology, Center for Electron Microscopy, MOE Key Laboratory of Artificial Micro- and Nano-structures, and Institute for Advanced Studies, Wuhan University, Wuhan, China. [11]These authors contributed equally: Jiajun Luo, Xiaoming Wang, Shunran Li, Jing Liu. *e-mail: yanfa.yan@utoledo.edu; jtang@mail.hust.edu.cn

Supplementary information for:

Efficient and stable warm-white emissive lead-free halide double perovskites

Jiajun Luo,[1†] Xiaoming Wang,[2†] Shunran Li,[1†] Jing Liu,[1†] Yueming Guo,[3] Guangda Niu,[1] Li Yao,[1] Yuhao Fu,[4] Liang Gao,[1,7] Qingshun Dong,[5] Chunyi Zhao,[6] Meiying Leng,[1] Fusheng Ma,[5] Wenxi Liang,[1] Liduo Wang,[5] Shengye Jin,[6] Junbo Han,[8] Lijun Zhang,[4] Joanne Etheridge,[3,9] Jianbo Wang,[10] Yanfa Yan,[2]* Edward H. Sargent,[7] Jiang Tang[1]*

[1]Sargent Joint Research Center, Wuhan National Laboratory for Optoelectronics (WNLO) and School of Optical and Electronic Information, Huazhong University of Science and Technology (HUST), Wuhan 430074, China

[2]Department of Physics and Astronomy and Wright Center for Photovoltaics Innovation and Commercialization, The University of Toledo, Toledo, Ohio 43606, United States

[3]Department of Materials Science and Engineering, Monash University, Victoria 3800, Australia

[4]Department of Materials Science and Engineering and Key Laboratory of Automobile Materials of MOE, and College of Materials Science and Engineering, Jilin University, Changchun 130012, China

[5]Key Lab of Organic Optoelectronics and Molecular Engineering of Ministry of Education Department of Chemistry, Tsinghua University, Beijing 100084, China

[6]State Key Laboratory of Molecular Reaction Dynamics and Collaborative Innovation Center of Chemistry for Energy Materials(iChEM), Dalian Institute of Chemical Physics, Chinese Academy of Sciences, Dalian 116023, China

[7]Department of Electrical and Computer Engineering, University of Toronto, 10 King's College Road, Toronto, Ontario, M5S 3G4, Canada.

[8]Wuhan National High Magnetic Field Center, Huazhong University of Science and Technology (HUST), Wuhan, Hubei 430074, P. R. China

---

[9]Monash Centre for Electron Microscopy, Monash University, Victoria 3800, Australia

[10]School of Physics and Technology, Center for Electron Microscopy, MOE Key Laboratory of Artificial Micro- and Nano-structures, and Institute for Advanced Studies, Wuhan University, Wuhan 430072, China

† These authors contributed equally to this work.

Supplementary Tables

Table S1. Crystallographic data for $Cs_2AgInCl_6$ and $Cs_2NaInCl_6$.

Formula	$Cs_2AgInCl_6$[61]	$Cs_2NaInCl_6$
FW	701.18	616.31
Crystal system, space group	Cubic, $Fm\overline{3}m$	Cubic, $Fm\overline{3}m$
a, Å	10.4780	10.5090
b, Å	10.4780	10.5090
c, Å	10.4780	10.5090
α, β, γ degree	90	90
V, Å^3	1150.36	1160.60

Table S2. Inductively coupled plasma optical emission spectrometer (ICP-OES) results of $Cs_2Ag_xNa_{1-x}InCl_6$.

To make our ICP-OES results more reliable, blank and standard samples were first used to calibrate the equipment. Then, we measured Na and Ag content in $Cs_2Ag_xNa_{1-x}InCl_6$ solution dissolved by HCl. This data was used to compute the Na/Ag ratio of $Cs_2Ag_xNa_{1-x}InCl_6$. Samples labels such as Ag9Na1 and Ag4Na6 mean the feeding molar ratio in the precursors are Ag:Na=9:1 and 4:6, respectively. By comparing the precursor molar ratio and composition of final products, we could observe a strong positive correlation between feeding ratio and final composition.

Sample Labels	Ag 328.068 (mg/L)	Na 589.592 (mg/L)	Ag (mmol/L)	Na (mmol/L)	ICP-OES results
Blank	0	0	0	0	/
Standard 1	1	1	0.01	0.04	/
Standard 2	3	3	0.03	0.13	/
Standard 3	5	5	0.05	0.22	/
Standard 4	10	10	0.09	0.44	/
Ag9Na1	60.15	0.97	0.56	0.04	$Ag_{0.93}Na_{0.07}$
Ag8Na2	75.38	2.96	0.70	0.13	$Ag_{0.84}Na_{0.16}$
Ag7Na3	55.59	4.53	0.52	0.20	$Ag_{0.72}Na_{0.28}$
Ag6Na4	60.23	8.49	0.56	0.37	$Ag_{0.60}Na_{0.40}$
Ag5Na5	73.13	12.52	0.68	0.54	$Ag_{0.55}Na_{0.45}$
Ag4Na6	64.17	19.61	0.59	0.85	$Ag_{0.41}Na_{0.59}$
Ag3Na7	62.61	29.95	0.58	1.30	$Ag_{0.31}Na_{0.69}$
Ag2Na8	56.05	41.19	0.52	1.79	$Ag_{0.22}Na_{0.78}$
Ag1Na9	33.98	51.55	0.32	2.24	$Ag_{0.12}Na_{0.88}$

We further applied ICP-OES to measure the concentration of Bi dopant in our products. Again, the facility is calibrated in advance. We measured Na, Ag, In and Bi content in $Cs_2Ag_xNa_{1-x}InCl_6$ with and without Bi doping, respectively. Clearly Bi incorporation into the final products is minuscule, however it significantly enhance the PLQY.

Sample Labels	Ag 328.068 (mg/L)	Na 589.592 (mg/L)	Bi 223.061 (mg/L)	In 230.606 (mg/L)	results
Blank	0	0	0	0	/
Standard 1	1	1	1	1	/
Standard 2	3	3	3	3	/
Standard 3	5	5	5	5	/
Standard 4	10	10	10	10	/
$Cs_2AgInCl_6$	87.1681	Not Found	Not Found	92.7809	AgIn
$Cs_2AgInCl_6$ doped Bi	168.676	Not Found	0.3031	179.375	$AgInBi_{0.0009}$
$Cs_2Ag_{0.60}Na_{0.40}InCl_6$	60.9637	8.6661	Not Found	108.1655	$Ag_{0.598}Na_{0.402}In$
$Cs_2Ag_{0.60}Na_{0.40}InCl_6$ doped with Bi	50.0147	7.1105	0.0556	88.7209	$Ag_{0.599}Na_{0.401}InBi_{0.0004}$

Table S3. Refinement Statistics for $Cs_2Ag_xNa_{1-x}InCl_6$ from Rietveld Refinements of High-Resolution Powder X-ray Diffraction Data.

Stoichiometric *x*	**a (Å)**	**Red. *x*2**	**wR**
0.08	10.48373(5)	4.49	3.91%
0.21	10.48741(5)	4.39	3.61%
0.28	10.49414(6)	4.35	3.46%
0.36	10.50094(6)	4.95	4.62%
0.4	10.50373(7)	4.67	4.90%
0.43	10.50979(7)	5.02	4.78%
0.53	10.51415(7)	4.39	3.64%
0.58	10.52052(5)	5.06	5.19%
0.74	10.52539(6)	4.97	4.59%

Table S4. The comparison of different representative white-emissive materials.

Materials	PLQY(%)	Reference
(N-MEDA)[$PbBr_4$]	1.5	[66]
(EDBE)[$PbBr_4$]	9.0	[67]
$C_4N_2H_{14}PbBr_4$	20.0	[68]
CdSe:Cu Nanocrystals	73	[69]
γ-AlOOH hybrid nanoplates	38	[70]
$Cs_2Ag_{0.60}Na_{0.40}InCl_6$	(86.2±5.0) %	This work

Supplementary discussion

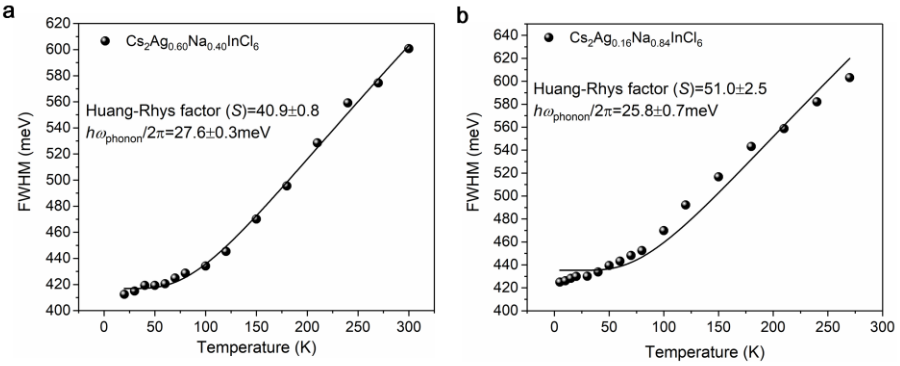

Figure S1| The fitting results of full width at half maximum (FWHM) as a function of temperature for a, $Cs_2Ag_{0.60}Na_{0.40}InCl_6$ **and b,** $Cs_2Ag_{0.16}Na_{0.84}InCl_6$. Note that only the PL FWHM derived from low temperature region can fit the equation well.

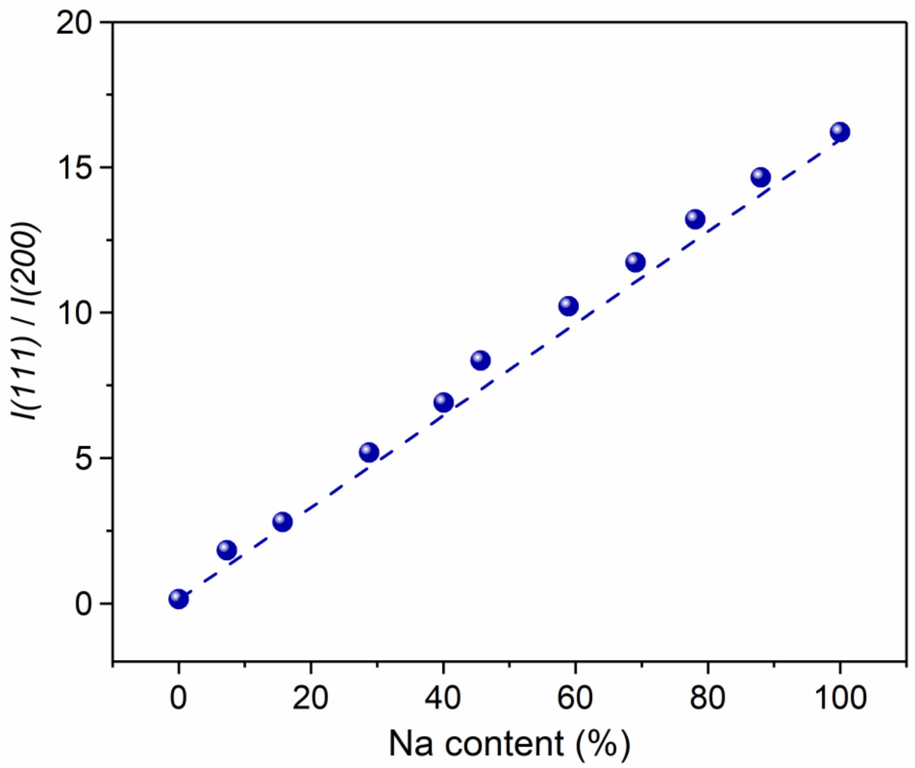

Figure S2| The (111) diffraction peak analysis of the $Cs_2Ag_xNa_{1-x}InCl_6$. The intensity ratio of (111) and (200) peak (I_{111}/I_{200}) versus the Na content.

The disorder of B and B' is commonly found in $A_2BB'O_6$ double perovskite materials, which produces antisite defects. Thus, the ordering of Ag, Na and In in $Cs_2Ag_xNa_{1-x}InCl_6$ deserved investigation. Fundamentally, the appearance of (111) peak attributes to the ordering arrangement of B(I) and B'(III) in halides double perovskites (Cs_2B(I)B'(III)X_6), and the theoretical relative intensity of (111) peak can be calculated based on the scattering factor of B(I) and B'(III), while each (200) plane contains both B(I) and B(III) cations and hence its diffraction peak intensity is insensitive to this ordering. Thereby, the relative intensity ratio of (111) and (200) peak (I_{111}/I_{200}) is a simple way to evaluate the degree of ordering in $Cs_2Ag_xNa_{1-x}InCl_6$. The theoretical intensity ratio of (I_{111}/I_{200}) of $Cs_2AgInCl_6$ and $Cs_2NaInCl_6$ are calculated to be 0.11 and 15.9[62],[63],[64], which is close to the experimental value of 0.14 and 16.2, indicating the perfect ordering arrangement of B(I) and B'(III). Besides, the intensity ratio of (I_{111}/I_{200}) increases linearly with the Na content (Supplementary Fig. S2), indicating the antisite defects are negligible (no additional disordering caused by Na alloying into $Cs_2AgInCl_6$ or equivalently Ag alloying into $Cs_2NaInCl_6$ in $Cs_2Ag_xNa_{1-x}InCl_6$ double perovskites using our slowly cooling crystallization method.

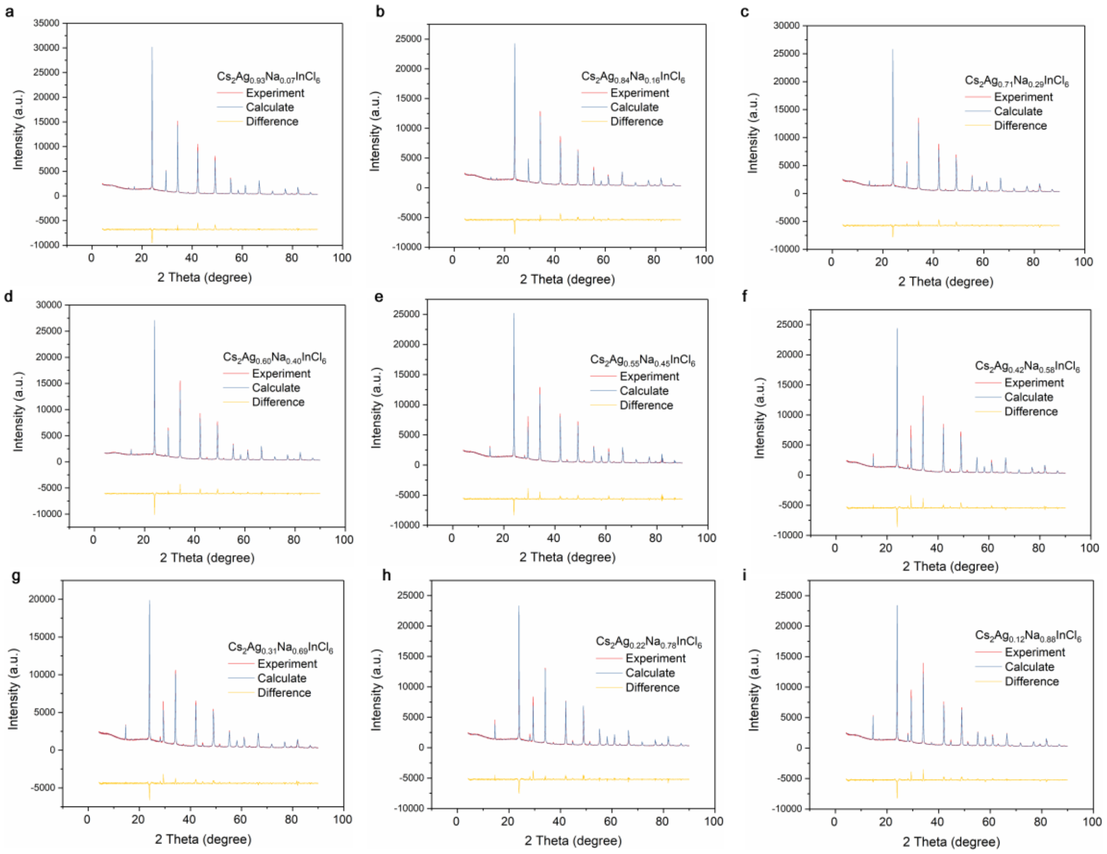

Figure S3| The high-resolution X-ray diffraction analysis and Rietveld refinements of the solid-solution series $Cs_2Ag_xNa_{1-x}InCl_6$. The structural parameters and refinement statistics are compiled in the Table S4.

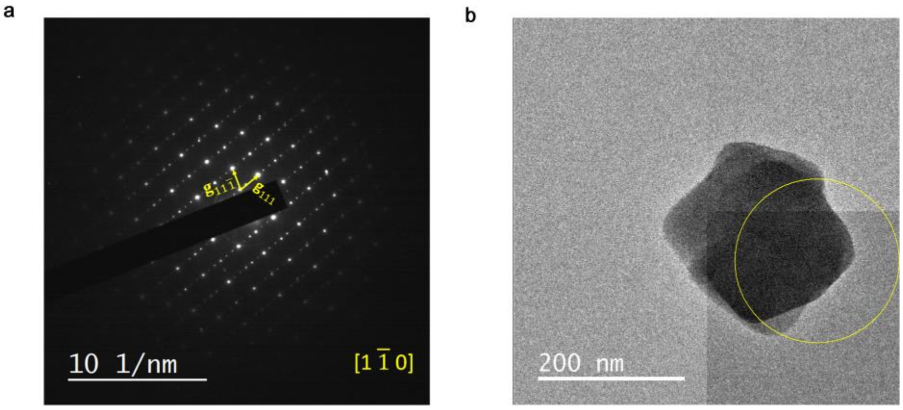

Figure S4| Electron microscopy and diffraction analysis of a small fraction of $Cs_2Ag_{0.60}Na_{0.40}InCl_6$. (a) A low dose selected area electron diffraction (SAED) pattern from the circled region in the (b) low dose TEM image of a crystal with the nominal composition $Cs_2Ag_{0.60}Na_{0.40}InCl_6$.

As shown in Supplementary Fig. S4a, the reciprocal lattice vectors $\mathbf{g_{111}}$ (the reciprocal lattice vector, indexed following the unit cell of $Cs_2AgInCl_6$) and $\mathbf{g_{11\bar{1}}}$ are labelled in the diffraction pattern, in which the pattern index has followed the double perovskite structure of $Cs_2Ag_2InCl_6$. (The bottom right quadrant of the image shows the inhomogeneous response of the CCD at low current densities but does not affect interpretation.) Superlattice reflections with a spacing of 1/3 $|g_{111}|$ are observed in the <111> direction (note that despite such a diffraction pattern satellite have been observed for multiple times, in many grains we can’t observe such a diffraction pattern). Given the nominal stoichiometry of the bulk crystal is 40% Na and $Cs_2AgInCl_6$ and $Cs_2NaInCl_6$ have nearly identical lattice constants, it is plausible the superlattice reflections arise from an ordering of the Na composition such that every one in three $(111)_{Ag}$ planes in $Cs_2AgInCl_6$ is replaced by a $(111)_{Na}$ plane. Based on such a model, the ordering between the two $[AgCl_6]$ and one $[NaCl_6]$ octahedral planes will be evident in half of the <110> projections and <110> SAED patterns such as shown in Figure S4, while it will not be visible in the other half.

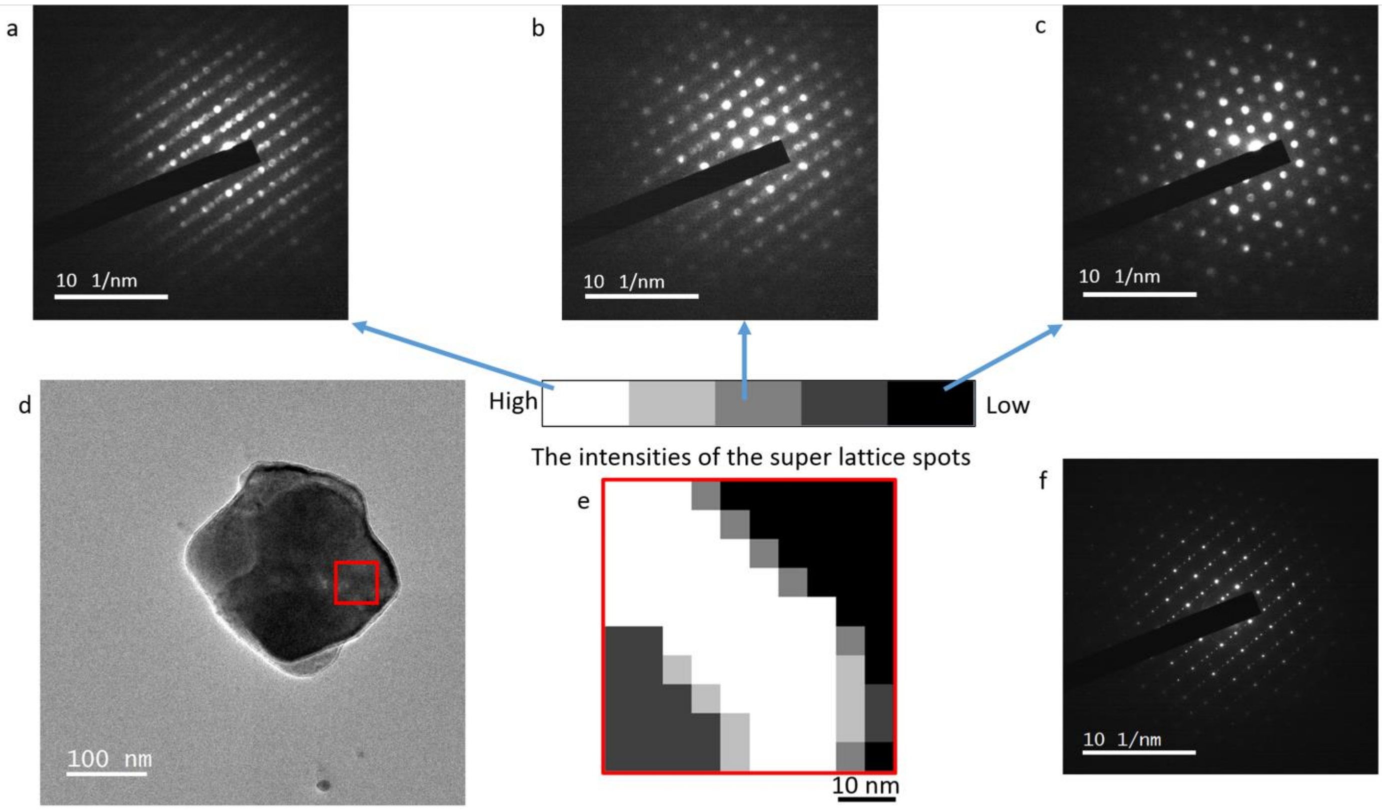

Figure S5| The ordering analysis of B(I) site in $Cs_2Ag_{0.60}Na_{0.40}InCl_6$. A set of 10 x 10 scanning nano-beam electron diffraction (SEND) patterns (e.g. a-c) were obtained from the labelled square region in (d). According to the total intensities of superlattice reflections, the scanned region was mapped in grey levels (e). The diffraction patterns obtained in the white-coloured area show the presence of superlattice reflections while those from the black areas show the absence of the superlattice reflections. (f) A selected area diffraction pattern was obtained from the whole scanned region before the SEND experiment.

We further used scanning electron nanobeam diffraction (SEND) to investigate whether the structure varies locally on the nanometer scale. SEND uses a nano-sized probe (in this case, ~5 nm with a slight convergence semi-ange of 1.6 mrad) to scan across the region of interest and records an electron diffraction pattern at each spot where the probe dwells. Moderately low dose conditions were used (1.6 pA/cm^2 with 0.1s dwell time). The SEND results imply that Na^+/Ag^+ is mainly randomly distributed at B(I) site but ordering, formation of superlattice, was observed for a small fraction in $Cs_2Ag_{0.60}Na_{0.40}InCl_6$. The superlattice spots are only observable for a small region (white region in Figure S5e), which is consistent with the absence of superlattice diffraction peaks at low angles even in our high resolution XRD results of $Cs_2Ag_{0.60}Na_{0.40}InCl_6$.

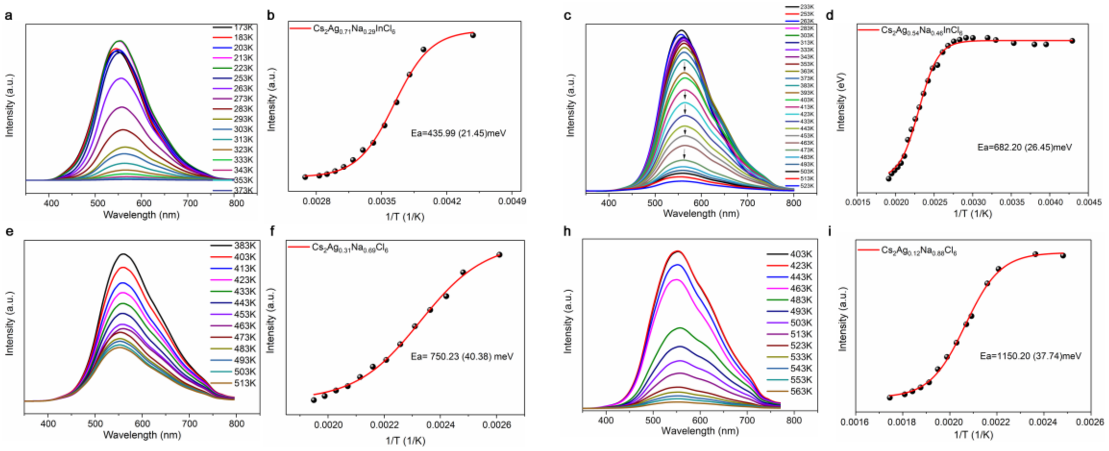

Figure S6| Temperature-dependent PL spectra of $Cs_2Ag_xNa_{1-x}InCl_6$ powder and the corresponding fitted results: a, b, $Cs_2Ag_{0.71}Na_{0.29}InCl_6$, **c, d,** $Cs_2Ag_{0.54}Na_{0.46}InCl_6$, **e, f,** $Cs_2Ag_{0.31}Na_{0.69}InCl_6$, **g, h,** $Cs_2Ag_{0.12}Na_{0.88}InCl_6$.

Clearly, the integrated PL intensity monotonically increased as the samples were cooled down because the defects that lead to nonradiative recombination loss at elevated temperature are deactivated at low temperatures, based on the following equation[65]

$$I(T) = \frac{I_0}{1 + A\exp(-E_b / k_B T)}$$

where I_0 and $I(T)$ are the PL intensity at 0 K and T K, respectively; A is a constant, E_b is the activation energy, k_B is Boltzman constant. By fitting the temperature dependent PL intensity, we could extract the activation energy in $Cs_2Ag_xNa_{1-x}InCl_6$ powders with varied Na content. Temperature-dependent XRD was carried out, as shown in Supplementary Fig. S7, to confirm no phase transition existed during the temperature range for PL analysis. As-calculated activation energy increases as Na content increase, suggesting the suppressed recombination loss and thermal quenching.

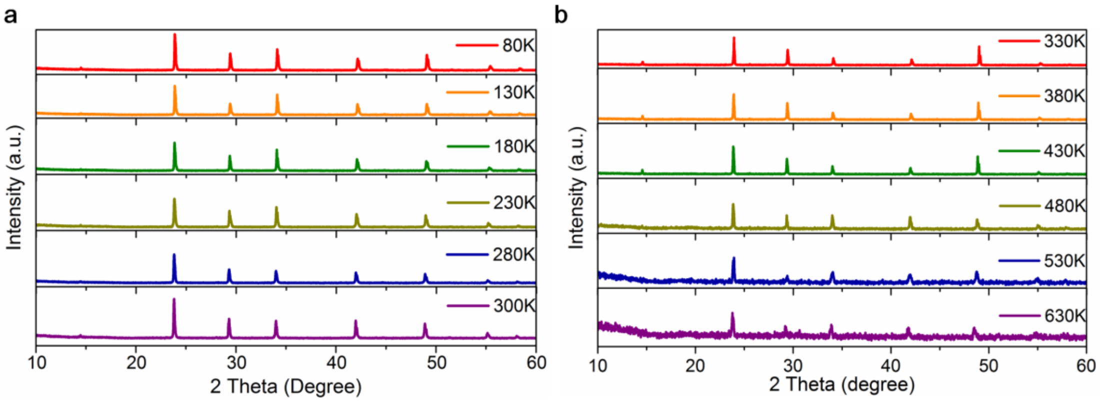

Figure S7| The temperature-dependent powder X-ray diffraction (XRD) patterns of the $Cs_2Ag_{0.60}Na_{0.40}InCl_6$ at a, 80K-300K and **b,** 330K-630K.

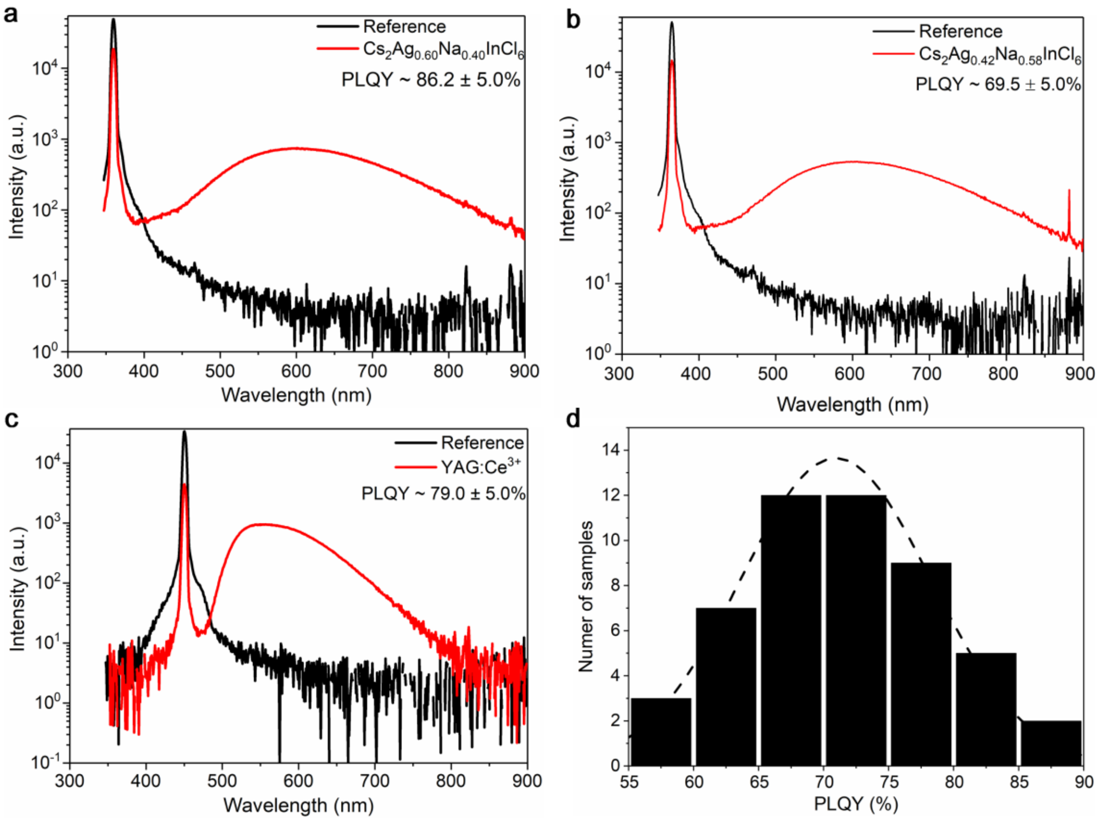

Figure S8| Characterization and calibration of the PLQYs of $Cs_2Ag_xNa_{1-x}InCl_6$. Excitation line of reference and emission spectrum of **a,** $Cs_2Ag_{0.60}Na_{0.40}InCl_6$, **b,** $Cs_2Ag_{0.42}Na_{0.58}InCl_6$, and **c,** commercial YAG:Ce^{3+} collected by an integration sphere. **d,** the reproducibility of the high PLQY samples.

PLQY calculation was based on the following equation[71]:

$$\tau_{QE} = \frac{I_{sample}}{(A_{reference} - A_{sample})}$$

Where A_{sample} and $A_{reference}$ are the absorption intensity of an integrating sphere with and without sample in a blank quartz vessel, respectively, and I_{sample} is the integrated emission intensity of samples collected by the same integrating sphere. PLQY of our $Cs_2Ag_xNa_{1-x}InCl_6$ powders were measured by ourselves, as well as by Fusheng Ma from Prof. Liduo Wang and Yong Qiu group, Department of Chemistry, Tsinghua University. Commercial YAG:Ce^{3+} phosphor was applied to calibrate our system (labelled PLQY 80~85%; measured PLQY (79.0±5.0)%), validating our PLQY results. Moreover, 50 batches of samples were measured to verify the reproducibility of our PLQY result: best~86.2%; average~71.0%, lowest~56.0%.

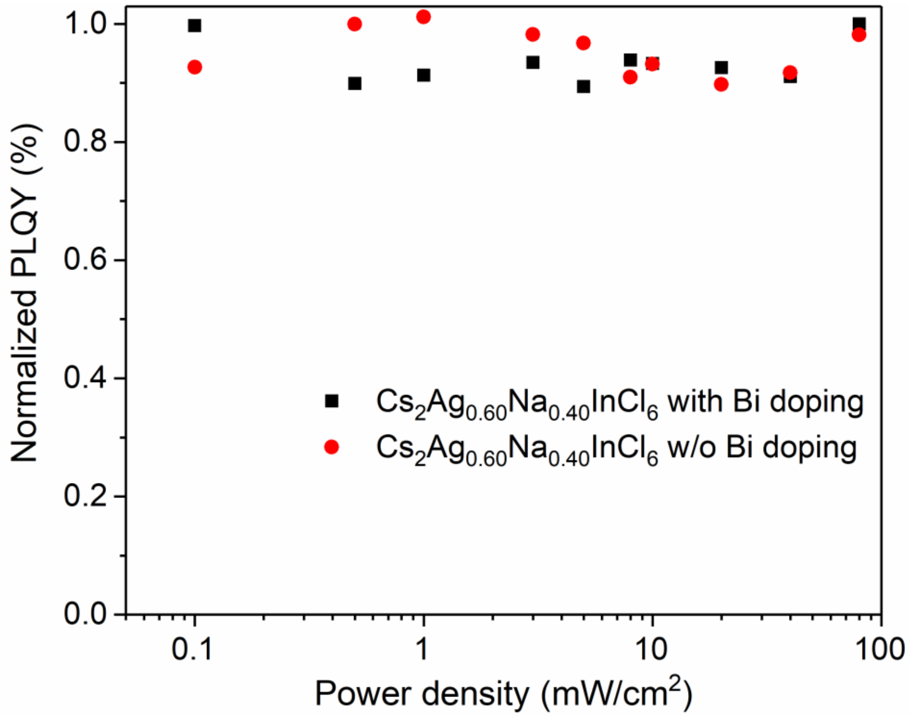

Figure S9| Pump-power-dependent PLQY measurement of $Cs_2Ag_{0.60}Na_{0.40}InCl_6$ with and without Bi doping.

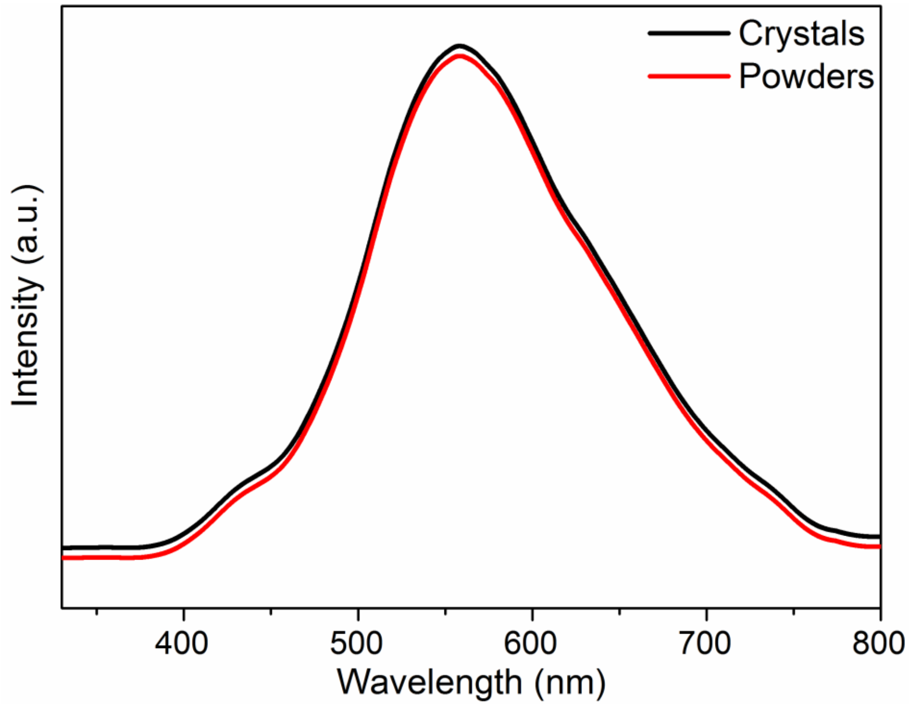

Figure S10| PL from crystals and ball-milled powder of $Cs_2Ag_{0.60}Na_{0.40}InCl_6$ at room temperature. It should be noted that powder was ball-milled from the same crystals, and all the other measurement parameters stayed the same.

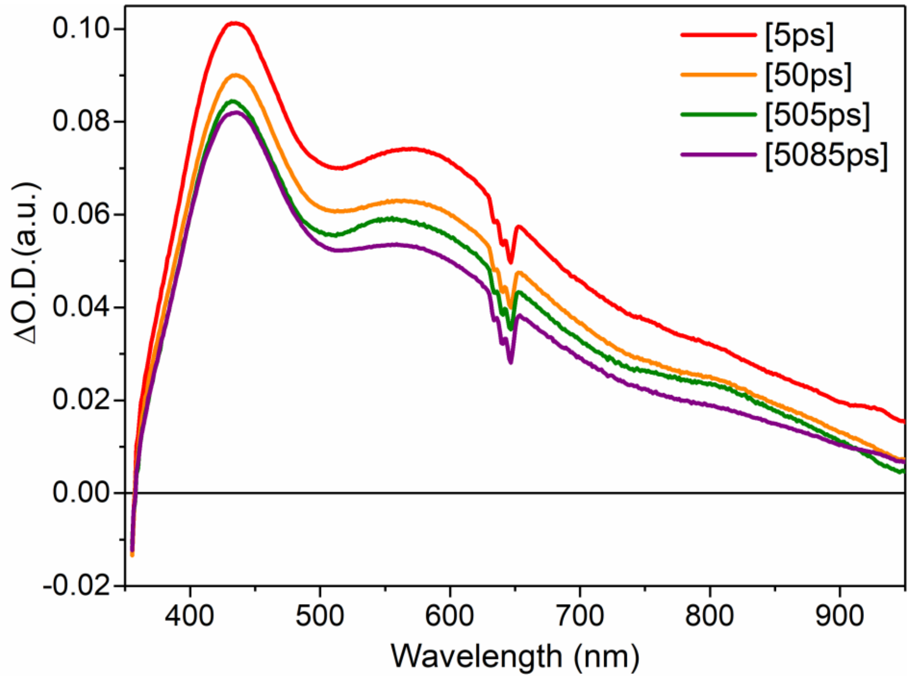

Figure S11| Details of transient (TA) absorption for $Cs_2Ag_{0.60}Na_{0.40}InCl_6$ excited by 325 nm-wavelength laser. TA spectra at different time delay for $Cs_2Ag_{0.60}Na_{0.40}InCl_6$ (laser pulse: 325 nm, 4μJ/cm^2), O.D., optical density. Photo-induced absorption is observed throughout the whole visible spectrum. The irregular peaks located at ~650 nm are from frequency doubling of the light source.

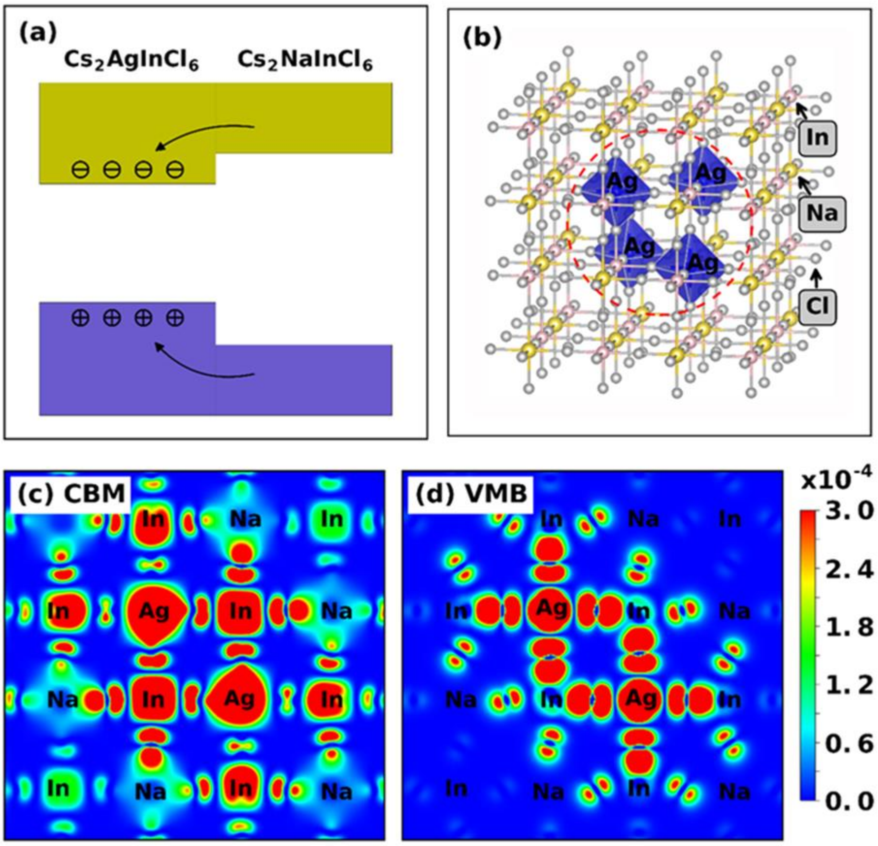

Figure S12|The theoretical calculation of Na alloyed $Cs_2AgInCl_6$ double perovskite. **a,** Calculated energy band alignment of the heterostructure formed by $Cs_2AgInCl_6$ and $Cs_2NaInCl_6$. The band gaps are calculated by the HSE06 functional. **b,** Structure model used in calculation: the $Cs_2AgInCl_6$ cluster containing four $AgCl_6$ octahedra embedded in the $Cs_2NaInCl_6$ matrix. **c, d,** The wave-function square plots of the conduction band minimum (CBM) and valence band maximum (VBM) states of the structure model in (b). The contour plots at the (100) plane are shown and the unit is electrons/Å^3. The main conclusion is that Na contributes neither to CBM nor to CBM.

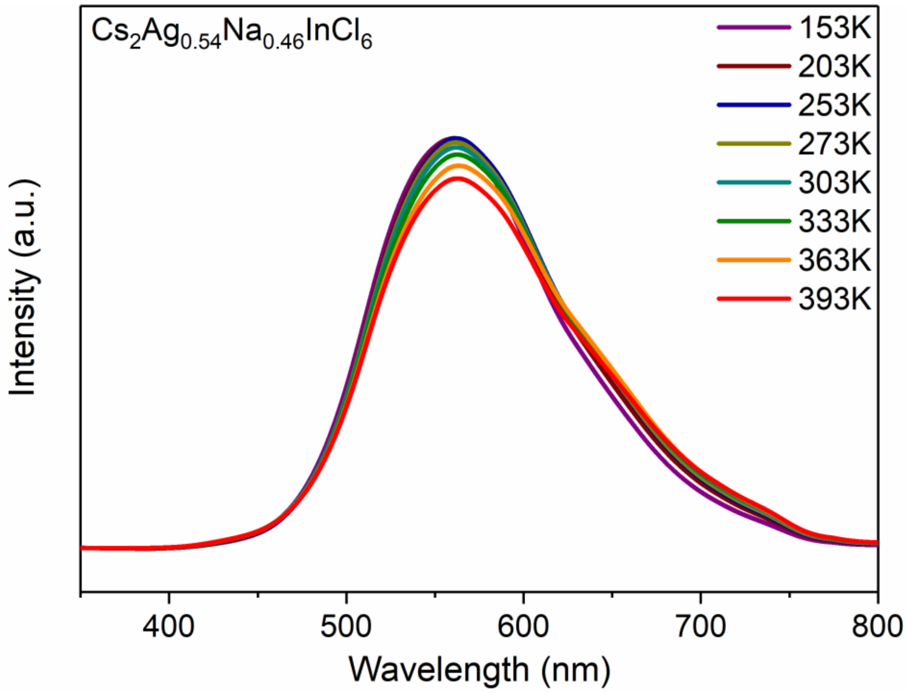

Figure S13| The PL spectra of $Cs_2Ag_{0.54}Na_{0.46}InCl_6$ at different temperature from 153 K to 393 K. The $Cs_2Ag_{0.54}Na_{0.46}InCl_6$ demonstrated very stable white emission between 153 K and 393 K and little PL quenching by heat.

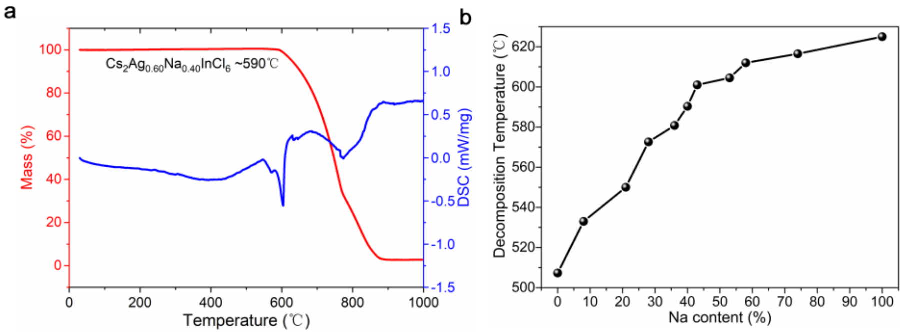

Figure S14| Thermal stability of $Cs_2Ag_xNa_{1-x}InCl_6$. a, Thermogravimetric analysis (TGA) and differential scanning calorimeter (DSC) analysis of the $Cs_2Ag_{0.60}Na_{0.40}InCl_6$ power. **b,** the decomposition temperature derived from TGA analysis of $Cs_2Ag_xNa_{1-x}InCl_6$ with different Na content.

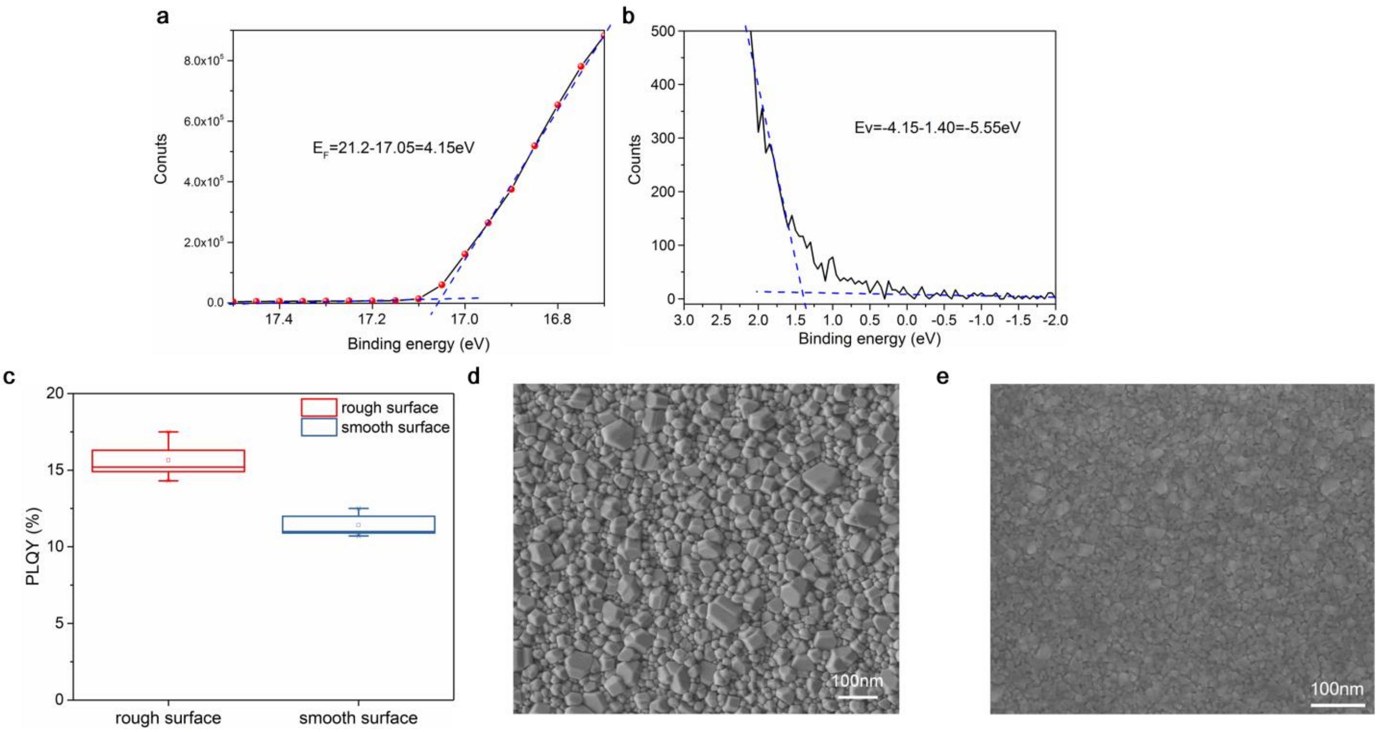

Figure S15| Fabrication and characterization of $Cs_2Ag_{0.60}Na_{0.40}InCl_6$ films. a, b, The ultraviolet photoelectron spectroscopy (UPS) results of 50 nm thick $Cs_2Ag_{0.60}Na_{0.40}InCl_6$ film. **c,** the PLQY of 100 nm $Cs_2Ag_{0.60}Na_{0.40}InCl_6$ film with different film morphologies. The scanning electron microscope (SEM) images of **d,** top-view SEM image of rough surface film and **e,** smooth surface film. The PLQY results of film should also consider the outcoupling effect[74].

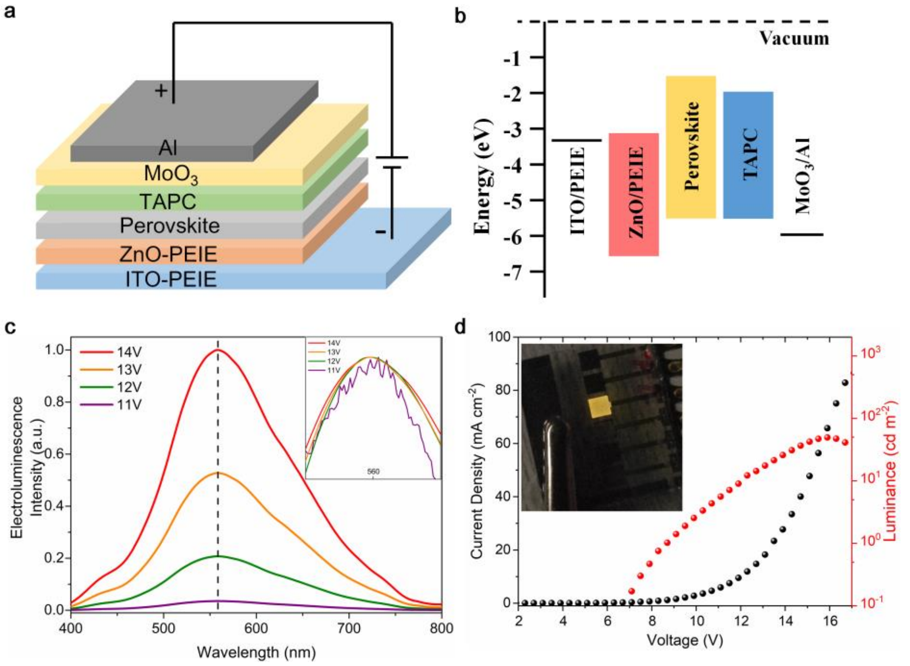

Figure S16| $Cs_2Ag_{1-x}Na_xInCl_6$ based electroluminescence devices. a, The electroluminescent device structure, glass/ PEIE modified ITO /PEIE modified ZnO(20 nm) / $Cs_2Ag_{0.60}Na_{0.40}InCl_6$ film(50 nm)/ TAPC(40 nm)/ MoO_3(8 nm)/ Al(100 nm), where PEIE is polyethylenimine, TAPC is 4,4'-Cyclohexylidenebis[N,N-bis(4-methylphenyl) benzenamine]. The band alignment of our EL devices is shown in supplementary Fig. S15. **b**, energy band diagram of $Cs_2Ag_{0.60}Na_{0.40}InCl_6$ LED device, and the band positions of ITO-PEIE, ZnO-PEIE, TAPC and MoO_3/Al are adopted from literature[72,73]. **c,** Electroluminescence spectra at an applied voltage of 11 V, 12 V, 13 V and 14 V, respectively. The inset is the normalized spectra. **d,** Dependence of current density and luminance on the driving voltage.

Note that the broadband emission cannot be attributed to the emission of TAPC because the PL emission peak of TAPC are located at 382 nm. To further verify this effect, EL emissions of pure TAPC was examined via the classical structure of ITO-PEIE/ZnO-PEIE/TAPC/MoO_3/Al. However, no visible light can be observed until they break down, indicating that the broadband emission was indeed from $Cs_2Ag_{0.60}Na_{0.40}InCl_6$. The EL spectra exhibited no bias dependence, an attractive nature enabled by the STE emission mechanism. We also measured the stability of our EL device inside glovebox, with the T_{50} lifetime being approximately 10 minutes operating at 50 mA/cm^2. High Joule heat and high driving voltage at low efficiency do work against stability, a point that calls for future work.

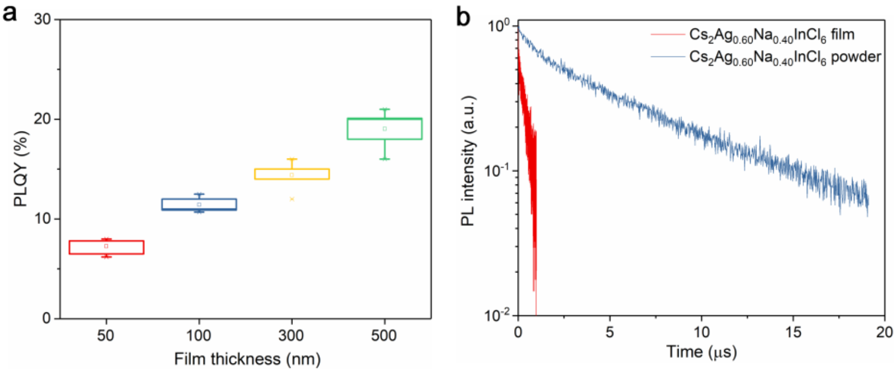

Figure S17| Limiting factors of our $Cs_2Ag_{0.60}Na_{0.40}InCl_6$ based EL devices. a, film thickness dependent PLQY results of $Cs_2Ag_{0.60}Na_{0.40}InCl_6$ film. **b,** the transient PL measurement of 100 nm thick $Cs_2Ag_{0.60}Na_{0.40}InCl_6$ films.

The performance of our electroluminescent device is low, and calls for further substantial improvement. First of all, high quality $Cs_2Ag_{0.60}Na_{0.40}InCl_6$ films should be produced. We explored various methods to deposit perovskite film, and identified thermal evaporation to be the most feasible one. Concentrated aqueous HCl solution is the only solvent that dissolves $Cs_2Ag_xNa_{1-x}InCl_6$ well, and spray-pyrolysis of this precursor solution often generate $Cs_2Ag_xNa_{1-x}InCl_6$ film with secondary phases and pin-holes. Careful composition control is imperative for the thermally evaporated film, and a post 5 mins' ambient exposure is found to be beneficial for the grain growth of $Cs_2Ag_xNa_{1-x}InCl_6$ film mainly through the assistance of moisture in the ambient. Despite intensive optimization, our $Cs_2Ag_{0.60}Na_{0.40}InCl_6$ films always show lower PLQY compared to their bulk counterparts (Fig. S17b), and the PLQY value is heavily dependent on the film thickness. The exact reason is not clear yet, and we suspect that severe non-radiative recombination through surface defects is probably responsible for PLQY decrease. For reference, thermally evaporated $Cs_4PbBr_6/CsPbBr_3$ film also show a much lower PLQY compared to its bulk counterpart [75], [76]. Moreover, the perovskite film exhibits some pinholes in Fig. S15d, e, which should be minimized to realize high efficiency EL device. Thereby, better film fabrication and passivation strategy should be developed to obtain a sub-30 nm thick $Cs_2Ag_{0.60}Na_{0.40}InCl_6$ film with much enhanced compactness and PLQY.

Second, due to the Na alloying, our $Cs_2Ag_xNa_{1-x}InCl_6$ has a reduced electronic dimensionality which means charge injection and transport is a problem. We believe that there remains pathways to high EL efficiency – for example, by reasoning in analogy with core-shell quantum dots (QDs) covered using long organic ligands. These too have low charge transport, yet have led to high-performing QD EL devices based on efficient injection into, and blocking of carrier overflow from, QD layers. For our current EL device, both the ZnO/PEIE electron transport layer and TAPC hole transport layer have some mismatches with perovskite layer, which needs further extensive optimization.

In sum, we see no fundamental limitations for the white emissive EL device based on $Cs_2Ag_xNa_{1-x}InCl_6$ film, and believe that more research should be carried out to achieve better device performance.

Supplementary Reference

61. Luo, J. *et al.* $Cs_2AgInCl_6$ double perovskite single crystals: parity forbidden transitions and their application for sensitive and fast UV photodetectors. *ACS Photonics* **5,** 398–405 (2017).
62. Volonakis. G. *et al.* $Cs_2InAgCl_6$: A new lead-free halide double perovskite with direct band Gap. *J. Phys. Chem. Lett.* **8,** 772-778 (2017).
63. Tran, T. T. *et al.* Designing indirect-direct bandgap transitions in double perovskites. *Mater. Horiz.* **4,** 688 (2017).
64. Knochenmuss, R., Reber, C., Rajasekharan, M. V., & Güdel, H. U. Broadband near-infrared luminescence of Cr^{3+} in the elpasolite lattices $Cs_2NaInCl_6$, Cs_2NaYCl_6, and Cs_2NaYBr_6. *J. Chem. Phys.* **85,** 4280-4289. (1986).
65. Chen, Z. *et al.* Photoluminescence study of polycrystalline $CsSnI_3$ thin films: Determination of exciton binding energy. *J. Lumin.* **132,** 345-349 (2012).
66. Dnhner, R. E., HoKe, T. K. & Karunadasa. I. H. Self-assembly of broadband white-light emitters. *J. Am. Chem. Soc.* **136,** 1718-1721 (2014).
67. Dnhner, R. E., Jaffe, A., Bradshaw, R. L. & Karunadasa. I. H. Intrinsic White-Light Emission from Layered Hybrid Perovskites. *J. Am. Chem. Soc.* **136,** 13154-13157 (2014).
68. Yuan, Z. *et al.* One-dimensional organic lead halide perovskites with efficient bluish white-light emission. *Nature Commun.* **8,** 14051 (2017).
69. Kim, J.-H. *et al.* White electroluminescent lighting device based on a single quantum dot emitter. *Adv. Mater.* **28,** 5093-5098 (2016).
70. Bai, X. *et al.* Efficient and tuneable photoluminescent boehmite hybrid nanoplates lacking metal activator centres for single-phase white LEDs. *Nature Commun.* **5,** 5702 (2014).
71. Zhou, C. *et al.* Luminescent zero-dimensional organic metal halide hybrids with near-unity quantum efficiency. *Chem. Sci.* **9,** 586-583 (2018).
72. Wang, N. *et al.* Perovskite light-emitting diodes based on solution processed self-organized multiple quantum wells. *Nature Photon.* **10,** 699-704 (2016).
73. Kim, H.-Y. *et al.* Transparent InP Quantum Dot Light-Emitting Diodes with ZrO_2 Electron Transport Layer and Indium Zinc Oxide Top Electrode. *Adv. Funct. Mater.* **20,** 3451-3461 (2016).
74. Richter, J. M. *et al.* Enhancing photoluminescence yields in lead halide perovskites by photon recycling and light out-coupling. *Nature commun.* **7,** 13941 (2016).
75. Ling, Y. *et al.* Composite perovskites of cesium lead bromide for optimized photoluminescence. *J. Phys. Chem. Lett.* **8,** 3266– 3271 (2017).
76. Quan, L. N. *et al.* Highly emissive green perovskite nanocrystals in a solid state crystalline matrix. *Adv. Mater.* **29,** 1605945 (2017).